Large sphere motion in a nonhomogeneous turbulent flow

Large sphere motion in a nonhomogeneous turbulent flow

Nathanaël Machicoane[1,3]**, Robert Zimmermann**[1,3]**, Lionel Fiabane**[1,3]**, Mickaël Bourgoin**[2]**, Jean-François Pinton**[1] **and Romain Volk**[1,4]

[1] Laboratoire de Physique de l'École Normale Supérieure de Lyon, CNRS UMR 5672, 46 Allée d'Italie, F-69007 Lyon, France
[2] Laboratoire des Écoulements Géophysiques et Industriels, CNRS/UJF/G-INP UMR 5519, BP53, F-38041 Grenoble, France
E-mail: romain.volk@ens-lyon.fr

Abstract

We investigate the dynamics of very large particles freely advected in a turbulent von Kármán flow. Contrary to other experiments for which the particle dynamics is generally studied near the geometrical center of the flow, we track the particles in the whole experiment volume. We observe a strong influence of the mean structure of the flow that generates an unexpected large-scale sampling effect for the larger particles studied. This phenomenon was not observed for neutrally buoyant particles of smaller yet finite sizes, in homogeneous and isotropic turbulence (Fiabane *et al* 2012 *Phys. Rev.* E **86** 035301). We find that particles whose diameter approaches the flow integral length scale explore the von Kármán flow nonuniformly, with a higher probability to move in the vicinity of two tori situated near the poloidal neutral lines. This preferential sampling is quite robust with respect to changes of varied parameters: Reynolds number, particle density and particle surface roughness.

[3] These authors contributed equally to this work.

[4] Author to whom any correspondence should be addressed.

1. Introduction

Solving the dynamics of a sphere of diameter d freely advected in a turbulent flow requires a knowledge of all the forces acting on it. The determination of these forces is a long-standing challenge. It has been solved to a large extent for particles much smaller than the dissipation (or Kolmogorov) length scale η [1, 2]. In this case, the equation governing the particle velocity **v** is determined once the fluid velocity **u** is known, as the forces are dominated by Stokes drag and added mass effects [3]. Very small neutrally buoyant particles (i.e. $d \leqslant \eta$) follow the flow dynamics and have been used as Lagrangian *tracers* [4–6]. But as soon as the particle diameter is of the order of or greater than the dissipation length scale, the particle is no longer a flow tracer and its dynamics changes radically. Experiments have shown that the dynamics of finite-size particles ($5 \leqslant d/\eta \leqslant 40$) deviates from that of tracers even when particles are neutrally buoyant. The variance of their acceleration $\overline{a_i^2}$ (i.e. of the forces acting on them) was indeed found to decrease with size as $d^{-2/3}$ [5, 7–9].

Very few studies have been carried out for particles with size comparable to the integral length scale [10–12], despite their potential importance for applied situations [13, 14]. It has recently been shown that such particles show a very intermittent dynamics of both translation and rotation. The probability density functions (PDFs) of their linear and angular velocities are almost Gaussian, while the PDFs of their acceleration for linear and angular motions reveal wide stretched tails. A coupling between rotation and translation develops, consistent with a Magnus (or lift) force [10].

We build on previous work and address the issue of the motion of large particles, setting aside the particle orientation and focusing only on trajectories. We consider in particular the influence of the large-scale (inhomogeneous) flow structure and its impact on the particle's dynamics. This complements recent studies [11, 12] which have focused on the local flow surrounding the particles, but ignoring the influence of anisotropy and inhomogeneity of the flow at large scales. Our motivation stems from the possibility that particles with sizes close to the integral scale may be sensitive to the kinetic energy injection details and hence the large-scale structure of the flow.

Our experiment is performed in a von Kármán flow (described in section 2), in which large particles are tracked optically. We show that as the particle diameters are increased to a fraction of the integral scale, they explore nonuniformly the flow volume: there is preferential sampling of specific flow regions (section 3). We then investigate Eulerian flow maps, as captured by the particles' motions (section 4), and connect with small-scale Lagrangian data (section 5) before discussing in detail features of the preferential sampling effect which is the main finding of this study (section 6).

2. Experimental setup

2.1. Turbulence generation

In this paper, we study the motion of particles in a von Kármán flow using the same setup as that detailed in [10, 15] and summarized in figure 1. The turbulent flow is generated in the gap between two counter-rotating discs of radius $R = 9.5$ cm, fitted with straight blades 1 cm in height. The flow domain between the discs and walls has a cubic shape with length $H = 20$ cm $\simeq 2R$—the cross section of the vessel is square since flat walls are used to minimize
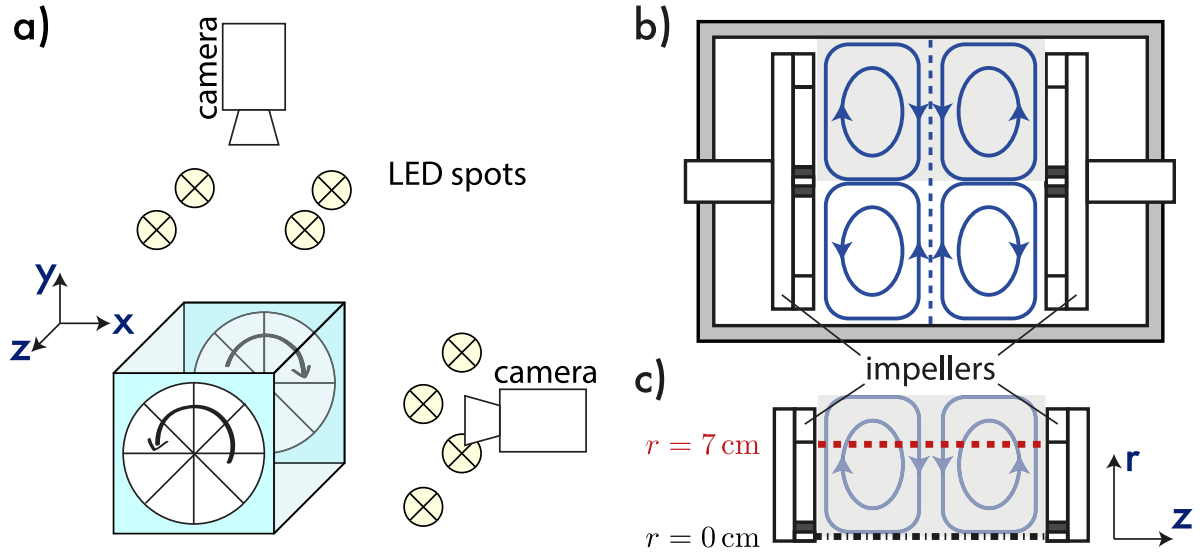
Figure 1. (a) The flow vessel and the optical setup. (b) Schematics of the mean flow structure. (c) Zoom of the half cross section used hereafter to plot maps of data averaged azimuthally; longitudinal profiles shown later are computed along the red dotted line, at $r = 7$ cm.

optical distortion. This type of von Kármán swirling flow has been used extensively in the past for the study of particle dynamics in fully developed turbulence (see Toschi *et al* [6] and references therein); at its center, its local characteristics approximate homogeneous turbulence, although it is anisotropic for large-scale quantities [16–19]. The fluid is set in motion near the two discs in the azimuthal θ-direction, creating two toroidal structures moving in opposite directions, with a strong shear at the center. A poloidal flow is formed as fluid is pumped along the axial z-axis toward the center of the discs and an opposite motion occurs along the walls. The combination of the r- and z-components forms recirculation cells called poloidal structures. It can be noted that the use of a square cross section pins the center shear layer in the $z = 0$ plane (mid-plane of the vessel) when the two impellers work at the same frequency, contrary to von Kármán flows generated in circular cross section vessels which can exhibit an instability and reversals for the shear layer (e.g. [20]).

The working fluid is a water–glycerol mixture whose density can be finely adjusted to the density of the PolyAmid spheres used here. The resulting mixture has a density of 1.14 g cm^{-3} and a dynamic viscosity of $\mu = 7.5 \times 10^{-3}$ Pa s at working temperature $\Theta = 20\,°\text{C}$. Temperature is maintained fixed by cooling plates at each end of the vessel. We estimate the energy injection rate ε using the formula $\varepsilon = (P_{\text{water}} - P_{\text{air}})/M$ where P_{water} and P_{air} are the total power consumption of the two motors in the working fluid and in air and M is the total mass of fluid. Subtracting the power used for air eliminates the friction losses, and yields an estimation of ε in good agreement with a local estimation based on the zero crossing of the Lagrangian acceleration autocorrelation function of tracer particles [9]. We also measured the fluctuating velocity $u' = \sqrt{(u^2_{i,\text{rms}})/3}$ in a smaller vessel with the same aspect ratio [21]. For a fully turbulent von Kármán flow, it is known that u' (or other velocities) scales as the disc tip velocities $2\pi R f_{\text{imp}}$ [9, 17] (R being the disc's radius), allowing us to extrapolate the value of u' for the vessel used in this paper (by multiplying the value of u' in the smaller vessel by the disc's

Table 1. Experimental parameters. f_{imp}: rotation frequency of the counter-rotating discs; ε: energy dissipation estimated from the electrical power consumption of the motors; $Re \equiv (2\pi R^2 f_{imp})/\nu$: Reynolds number computed using the discs tip velocity; $R_\lambda = \sqrt{15 \times 2\pi L_{int}^2 f_{imp}/\nu}$: Reynolds number based on the Taylor microscale, with $L_{int} = 3$ cm the estimated integral length scale; $\tau_\eta \equiv (\nu/\varepsilon)^{1/2}$: Kolmogorov time scale; $f_{sampling}$: cameras sampling frequency; $\eta \equiv (\nu^3/\varepsilon)^{1/4}$: Kolmogorov length scale and d/η: the length ratio between the particle diameter and the dissipation scale. The particles diameter ranges between $1/5\,L_{int}$ and $4/5\,L_{int}$.

f_{imp} (Hz)	ε (W kg^{-1})	Re	R_λ	τ_η (ms)	$f_{sampling}$ (Hz)	η (μm)	d/η
2	0.58	17 300	161	3.4	800	148	[40–162]
3	1.89	26 000	197	1.9	1000	110	[54–218]
4	4.35	34 700	228	1.2	1500	89	[67–268]

radii ratio). From these estimates of ε and u', we define the integral length scale of the flow as $L_{int} = u'^3/\varepsilon$, being approximatively 3 cm for the flow considered here. Table 1 summarizes the flow parameters.

2.2. Particle tracking

We study the Lagrangian dynamics of PolyAmid spheres with diameters $d = [6, 10, 18, 24]$ mm (accuracy 0.01 mm, Marteau and Lemarié, France) and a density $\rho_{PA} = 1.14$ g cm^{-3}. The particles are *large* in this study, meaning that their diameter is of the order of the integral scale. The motion of the particles is tracked using two high-speed video cameras (Phantom V.12, Vision Research, 1 Mpix@6 kHz) recording synchronously two views at approximately $90°$. The flow is illuminated by high-power light-emitting diodes (LEDs) and sequences of 8 bit grayscale images are recorded at a rate $f_{sampling}$ ranging from 800 to 1500 frames s^{-1} depending on the rotation frequency of the impellers (see table 1). Both cameras observe the measurement region with a resolution of 725×780 pixels, covering a volume of $20 \times 20 \times 15$ cm^3 (the shortest distance being between the impellers). Hence, the particles cover between 20 and 120 pixels depending on their size. The cameras are located approximately 2 m away from the apparatus and small variations of the particles' sizes are observed as they move in the flow. Track durations are limited by the camera's on-board memory which stores about 14 000 frames. Given this limitation, for each particle and rotating frequency, we record more than 4000 trajectories whose durations are of the average order of 0.7 times the discs turnover time (taken as the inverse of the disc's rotating frequency). A previous study [22] asserts that these frame rates allow good confidence in acceleration measurements, as the particles acceleration is correlated over approximatively 40 frames.

Great experimental care is taken in the illumination of the flow so that the particles' luminosity is uniform, and shadows and reflections are negligible. Particle detection and tracking is carried out using Matlab® routines and its image and signal processing toolboxes. For each acquisition, we compute the background as the average of an equally distributed subset of its images. We then subtract the background for each frame and threshold to detect the blobs corresponding to particles.
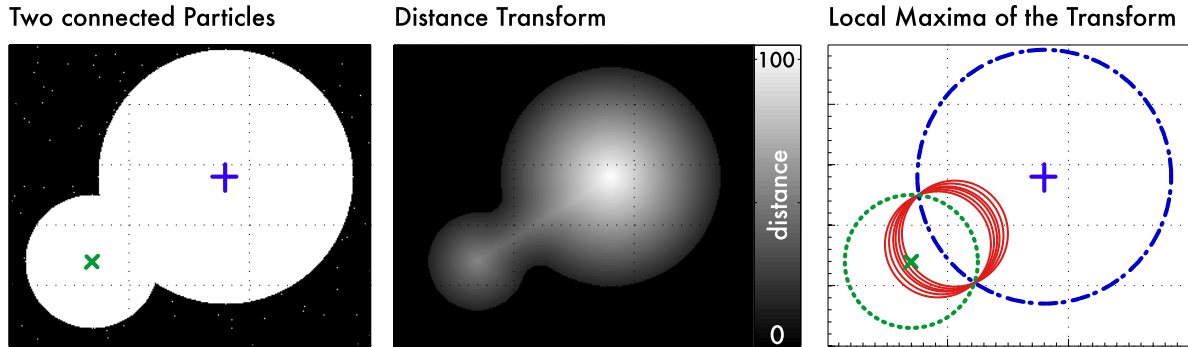
Two connected Particles   Distance Transform   Local Maxima of the Transform

Figure 2. Sketch of the blob-splitting technique. Overlapping particles form a blob (left). The distance transform then returns for each white pixel the Euclidean distance to the closest black pixel (middle). The local maxima of the distance transform are possible particle positions with their associated radii. Often, more maxima than particles are detected and one has to remove artifacts: starting from the largest radius one iteratively excludes wrong detections which are within a bigger particle (solid red circles, right). One finally obtains the position (x, y) and radius r of the disentangled particles (dotted green and dashed blue circles).

For round, unconnected blobs we directly save their location (x, y) on the image together with their diameter (in pixels). Connected blobs are split using the maxima of the distance transform [23] of the blob as sketched in figure 2; the resulting disentangled positions and diameters are then separately stored. Finally, a standard stereo-matching technique is performed to obtain each particle position in 3D, using Tsai's [24] camera model and calibration technique. If multiple particles are present in the flow (in order to optimize the experiments and obtain larger statistics), the track assembly is sometimes not straightforward. The main difficulties are removed by the following three steps. (i) Sort the detected particles by diameter. (ii) Connect particles of identical size using a nearest-neighbor algorithm with a short interpolation scheme (namely, gaps of less than seven times the Kolmogorov time scale are interpolated, corresponding to the number of frames between 15 and 20 depending on the turbulence level and frame rate). Due to their large size, particles optically disappear when they enter the projected 'shade' of another particle. We therefore apply the algorithm suggested in [25] to reconnect tracks; it enforces continuity for both position and velocity. (iii) Identify and eliminate outliers with a least-square spline.

We can note also that only six particles at a time were in the experimental setup and no collisions between particles were observed, which is indeed expected in such a delicate situation.

3. Nonuniform sampling

Neutrally buoyant particles, with inertial range sizes ($D \sim [10 - 20]\eta$), are known to not form clusters in homogeneous turbulence [26], leading to a homogeneous sampling of the flow. However, it has not yet been investigated whether this is still true when particles are freely advected in a flow with a mean structure and nonhomogeneous properties, especially when particles have diameters of the order of the largest flow eddies. This is the question addressed in this section.
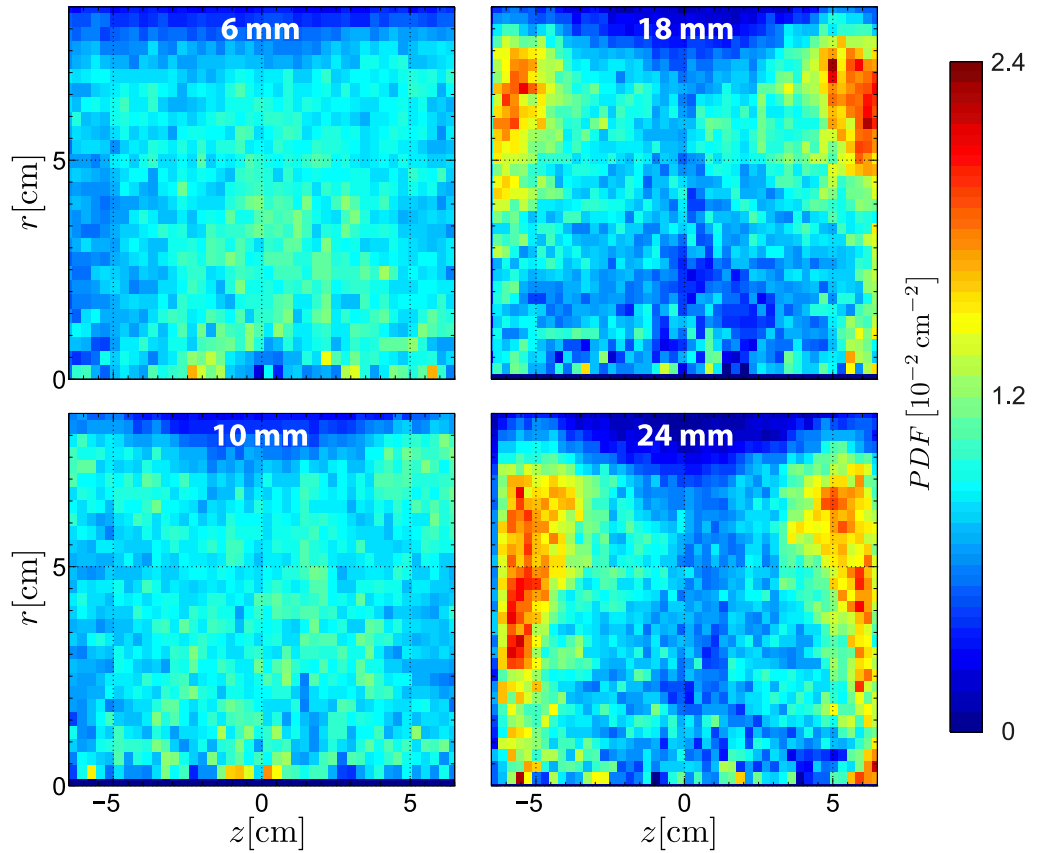
Figure 3. Maps of the PDFs of position for different particle diameters. On the left-hand side, the flow is homogeneously explored by the smaller particles (6 and 10 mm) whereas the larger particles (18 and 24 mm) on the right-hand side move preferentially near the impellers. Data are from experiments at $f_{imp} = 4$ Hz.

To answer this question, we first compute the stationary PDF of the particle positions $P(r, \theta, z)$ in cylindrical polar coordinates, and show results for the axisymmetric part of the PDFs, denoted $\langle P \rangle_\theta (r, z)$, in figure 3. Results are displayed in a half cross section of the vessel, with the impellers on each side (at $z = \pm 10$ cm) and the rotation axis in the center, as sketched in figure 1(c).

As clearly shown in figure 3, two very different cases are observed depending on whether the particles are smaller (6 and 10 mm, left-hand side in figure 3) or larger (18 and 24 mm, right-hand side in figure 3). Particles smaller than 10 mm explore the flow homogeneously with a probability almost uniform in a meridian plane. Such is not the case for larger particles. Particles with 18 and 24 mm diameters do not explore the flow uniformly, the probability density of finding the particle with $\parallel z \parallel \geqslant 4$ cm being twice larger than the corresponding value for $\parallel z \parallel \leqslant 4$ cm. From a geometric point of view, analyzing the maps, one finds that larger particles avoid the central part of the flow, and move preferentially in two tori with a large radius $R_T \simeq 6$ cm, located 5 cm away from the mid-plane, the discs location being at $z = \pm 10$ cm.

This development of a preferential flow sampling for large particles is a rather unexpected observation. Before further analysis, we need some insight into the properties, Eulerian and Lagrangian, of the carrier flow. In particular, it is of importance to correlate the probability maps with the mean and fluctuating velocity field maps.
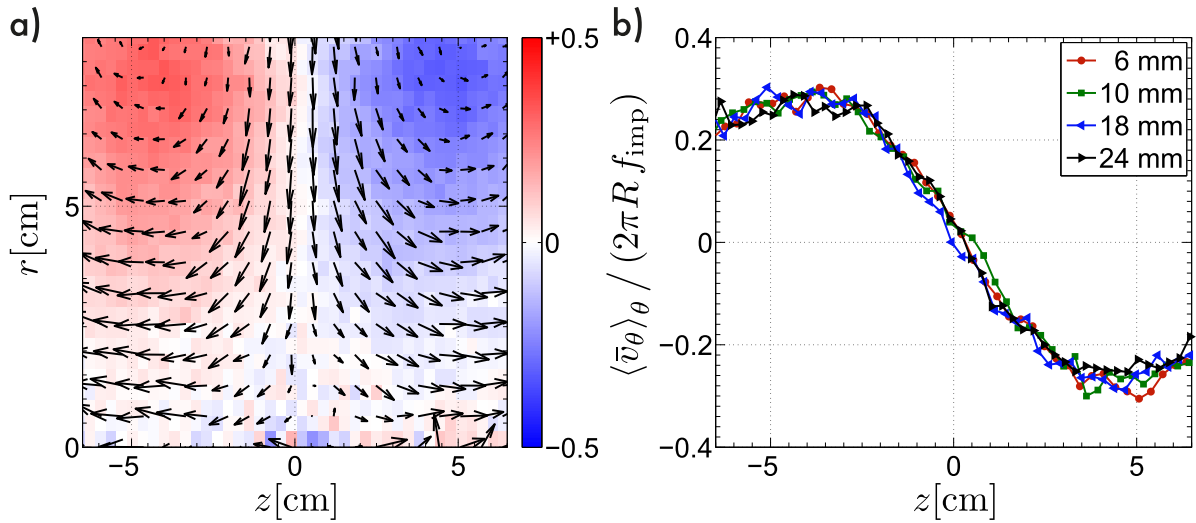
Figure 4. (a) Half cross section of the reconstructed Eulerian mean velocity field normalized by the large-scale driving $U = 2\pi R f_{imp}$. Arrows indicate the poloidal z- and r-components; colors show the azimuthal θ-component. Data obtained with a 6 mm particle at $f_{imp} = 4$ Hz. (b) Axial profile of the mean azimuthal velocity for particles with diameters between 6 and 24 mm (normalized by the disc tip speed $U = 2\pi R f_{imp} \simeq 2.4$ m s^{-1}) at $f_{imp} = 4$ Hz.

4. Eulerian maps

We discuss here Eulerian flow characteristics, as reconstructed from the Lagrangian motion of the particles, with emphasis on the influence of the particle sizes.

4.1. Mean velocity field

The 3D particle tracking yields a set of particle trajectories each containing the temporal evolution of Lagrangian velocity $\mathbf{v}_L$ and acceleration $\mathbf{a}_L$ at the particle position $\mathbf{x}(t)$. Based on this ensemble of trajectories and for each type of particle, one may define an effective Eulerian flow field $\mathbf{v}_E(r, \theta, z, t)$ by an Eulerian conditioning of the Lagrangian dataset. Assuming ergodic dynamics, one then obtains a mean velocity field $\overline{\mathbf{v}}_E(r, \theta, z) = (\overline{v}_r, \overline{v}_\theta, \overline{v}_z)$ and the rms fluctuations of each velocity component (v_r^{rms}, v_θ^{rms}, v_z^{rms}).

Figure 4(a) shows the map, obtained for the 6 mm particles, of the axisymmetric part of the reconstructed Eulerian velocity field $\langle \overline{\mathbf{v}}_E \rangle_\theta (r, z)$. Although 6 mm particles are not strictly flow tracers, one recognizes in figure 4(a) the mean structure characteristic of the counter-rotating von Kármán flow: an antisymmetric toroidal component $\langle \overline{\mathbf{v}}_\theta \rangle_\theta$ with respect to the mid-plane (colors) and a poloidal flow ($\langle \overline{\mathbf{v}}_r \rangle_\theta$, $\langle \overline{\mathbf{v}}_z \rangle_\theta$) showing two recirculation cells (arrows).

In order to study the influence of the particle diameter, we show the evolution of the mean toroidal component $\langle \overline{v}_\theta \rangle_\theta$ as a function of z at a given radius $r_0 = 7$ cm (along the red dotted line in figure 1). This location has been chosen such that the mean azimuthal velocity is significantly larger than any possible bias due to measuring incertitudes or lack of statistics. As depicted in figure 4(b), all profiles collapse onto the same curve. This surprising finding is very robust with respect to both velocity components and profile locations, provided the mean velocity is
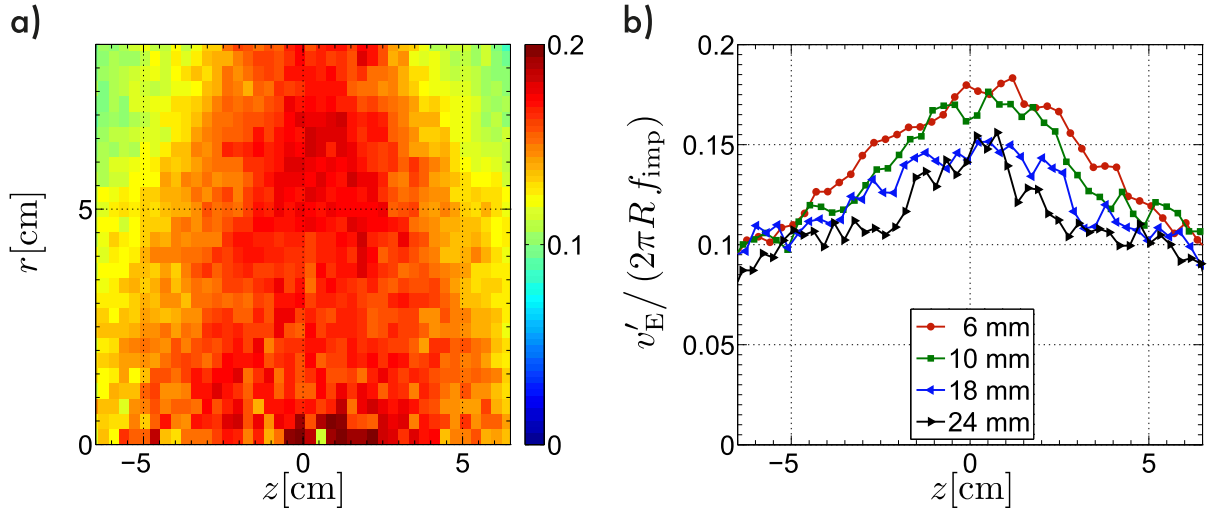
Figure 5. (a) Half cross section of the normalized fluctuating velocity $v'_E(r, z)/(2\pi R f_{imp})$ for 6 mm particles. (b) Longitudinal profile at $r = 7$ cm for increasing particle diameters. Data are from experiments at $f_{imp} = 4$ Hz.

strong enough. It means that neutrally buoyant particles follow the same mean flow independent of their size. Incidentally, it also means that given enough statistics, in such a free shear flow for which the bulk flow properties only vary smoothly, one may reconstruct the Eulerian mean velocity field from the trajectory of a single neutrally buoyant particle, whatever its diameter!

4.2. Fluctuating velocity field

We now consider the velocity fluctuation v'_E defined as

$$v'_E(r, z) = \left(\frac{\langle (v_r^{rms})^2 \rangle_\theta + \langle (v_\theta^{rms})^2 \rangle_\theta + \langle (v_z^{rms})^2 \rangle_\theta}{3} \right)^{1/2} = \left(\sum_{i=r,\theta,z} \frac{\langle (v_i^{rms})^2 \rangle_\theta}{3} \right)^{1/2}. \quad (1)$$

The resulting map and profiles are shown in figure 5, computed for the smallest particles with diameter 6 mm. A first observation is that the velocity fluctuations are strongly inhomogeneous. This is consistent with observations made with tracer particles (e.g. laser Doppler velocimetry results [27]). Fluctuations are larger near the rotation axis, close to the mid-plane and diminish where the toroidal component is the strongest. Again, these results tend to show that 6 mm particles, but not tracers, have a dynamics that correctly portrays the Eulerian flow [17].

Studying the longitudinal profiles, one observes in figure 5(b) that all have a similar shape, with higher fluctuations at the center (in or near the shear layer) than closer to the impellers. In contrast to the mean velocity, there is a clear sorting of the profiles especially in the central part of the vessel, where the normalized rms velocity $v'_E/(2\pi R f_{imp})$ decreases by over 10% when the particle diameter increases from 6 to 24 mm. This observation is robust for any location of the profile along the r-axis in the volume although it may vary in amplitude across the (r, z) plane. This decrease of the velocity fluctuations with increasing particle diameter differs from what has been reported for particles with diameters close to the dissipation scale [7, 9] (for which sizes d/η were in the range [1–45] and [12–26], respectively). Although part of those
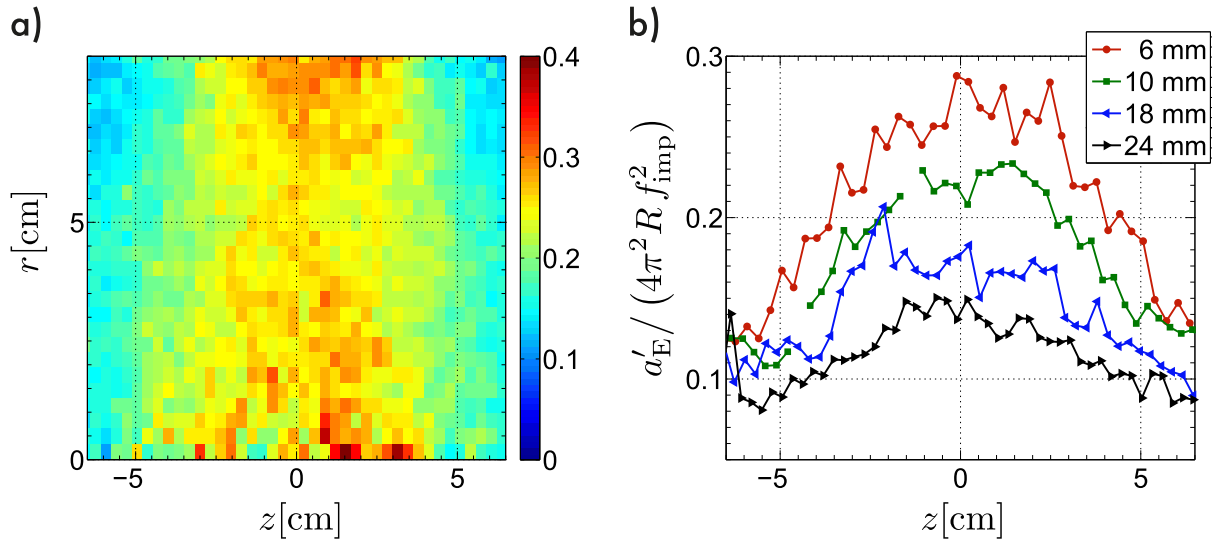
Figure 6. (a) Half cross section of the normalized fluctuating acceleration $a'_E(r, z)/(4\pi^2 R f_{imp}^2)$ for a 6 mm particle. (b) Longitudinal profile at $r = 7$ cm for increasing particle diameters. Data are from experiments at $f_{imp} = 4$ Hz.

measurements were carried out in the central region of the same turbulent flow, no dependence of the rms velocity on the particle diameter was observed.

As a partial explanation, one may recall that eddies with sizes of the order of the integral scale contain much more kinetic energy than those in the near dissipative range. Thus particles of integral sizes may average fluid fluctuations with a larger impact than is done by particles closer to the dissipation scale.

4.3. Accelerations

Following the above observations, we now consider the accelerations (at Eulerian fixed points) of the particles. Lagrangian studies have shown that this quantity is quite sensitive to particle sizes [5, 7–9]. We define the acceleration fluctuation

$$a'_E(r, z) = \left(\sum_{i=r,\theta,z} \frac{\langle (a_i^{rms})^2 \rangle_\theta}{3} \right)^{1/2}. \tag{2}$$

The corresponding maps and profiles are shown in figure 6. One observes that the acceleration fluctuations are much higher near the mid-plane of the vessel than to the sides where the mean flow is stronger. This is in agreement with previous observations on velocity, even though high acceleration fluctuations seem to be more localized at the center of the vessel even for small radii. As is already known for smaller particles [7–9], we observe in figure 6(b) a stronger decrease of acceleration magnitude when increasing the particle diameter than what was observed for velocity fluctuations. Although profiles seem to have a similar shape, a'_E is divided by 2 when size is increased fourfold. This is a stronger decrease than what was observed for particles of sizes in this inertial range; it will be further investigated together with its Reynolds number dependence in section 5. We note that the bell shape for the acceleration profile, with a larger value near the mid-plane ($z = 0$), is similar to local measurements of

dissipation ε, as computed from hot wire measurements by Zocchi *et al* [28] in a von Kármán of helium. It is consistent since Lagrangian accelerations of flow tracers are related to dissipation by $a_{\mathrm{rms}} \sim \varepsilon^{3/4} \nu^{-1/4}$.

5. Lagrangian quantities

In an inhomogeneous flow, the particles' mean and fluctuating quantities in their Lagrangian motion are also of interest, eventually to be connected to the known behavior of Lagrangian *tracers*. This may be done in two ways; the first is to compute 'standard' Lagrangian estimates using the Lagrangian velocity $\mathbf{v}_{\mathrm{L}}$ and acceleration $\mathbf{a}_{\mathrm{L}}$. They can be split into an ensemble average plus a fluctuating quantity ($\mathbf{v}'_{\mathrm{L}}, \mathbf{a}'_{\mathrm{L}}$) with rms values ($v_{i,\mathrm{L}}^{\mathrm{rms}}, a_{i,\mathrm{L}}^{\mathrm{rms}}$), $i = r, \theta, z$. A second possibility is to use the same Eulerian conditioning as that in the previous section, since large particles do not sample the flow uniformly. One then makes use of the position PDFs ($P(r, \theta, z)$) and defines the rms values of velocity (or acceleration) components as

$$v_{i,\mathrm{LE}}^{\mathrm{rms}} = \left(\iiint \mathrm{d}r\, \mathrm{d}\theta\, \mathrm{d}z\, r\, P(r, \theta, z)\, (\overline{v}_i(r, \theta, z))^2 \right)^{1/2}, \quad i = r, \theta, z. \tag{3}$$

The subscript 'LE' emphasizes here that one wishes to estimate the Lagrangian fluctuations taking into account the nonuniformity of the sampling in the Eulerian space[5].

Results for the normalized Lagrangian rms velocity $v_{\mathrm{L}}^{\mathrm{rms}}/(2\pi R f_{\mathrm{imp}})$ and acceleration $a_{\mathrm{L}}^{\mathrm{rms}}/(4\pi^2 R f_{\mathrm{imp}}^2)$ are displayed in figures 7(a) and (b), together with the corresponding normalized Eulerian velocity $v_{\mathrm{LE}}^{\mathrm{rms}}/(2\pi R f_{\mathrm{imp}})$ and acceleration $a_{\mathrm{LE}}^{\mathrm{rms}}/(4\pi^2 R f_{\mathrm{imp}}^2)$ in figures 7(c) and (d). This normalization collapses the velocity measurements made at different rotation rates of the driving discs. It is characteristic of a fully turbulent regime for which velocity mean and fluctuating quantities are proportional to the large-scale forcing [9, 17, 27].

However, anisotropy and characteristic values differ depending on the way estimates are computed. Indeed, the direct Lagrangian estimate $v_{\mathrm{L}}^{\mathrm{rms}}$, for which ensemble averaged velocity decreases to zero in a bounded flow, incorporates mean flow contribution into the fluctuations. One then finds that $v_{i,\mathrm{L}}^{\mathrm{rms}}$ is always larger than its corresponding component $v_{i,\mathrm{LE}}^{\mathrm{rms}}$. This is particularly clear for the toroidal component $v_{\theta,\mathrm{L}}^{\mathrm{rms}}$, found to be much larger than any other velocity component because of the added contribution from the mean azimuthal velocity, an antisymmetric quantity with respect to the z coordinate. When the mean flow contribution is removed in figure 7(c), the measured anisotropy is in better agreement with previous observations in von Kármán flows [5, 27]. We also note that the anisotropy seems to decrease with increasing particle size.

Contrary to velocity fluctuations, acceleration fluctuations—figures 7(b) and (d)—are very similar for all components and there is less influence from the methods used for computing the estimated rms (L or LE). This reduction of anisotropy for small-scale quantities such as the acceleration may be as expected, and is in agreement with measurements reported in the literature (e.g. [5, 16]) for Lagrangian *tracers*. Concerning the evolution with Reynolds number, one finds that particle acceleration is correctly normalized by the large-scale acceleration $4\pi^2 R f_{\mathrm{imp}}^2$ (also shown in [22]). This differs from the scaling $a^{\mathrm{rms}} \sim \varepsilon^{3/4} \nu^{-1/4}$ observed for

---

[5] Technically, rms values are computed by removing the local axisymmetric part of the mean velocity (or acceleration) at the particle position before computing $v_{\mathrm{LE}}^{\mathrm{rms}}$ as a standard deviation of the dataset. It ensures that all grid points are weighted by the time that particles spent at specific locations in the flow.
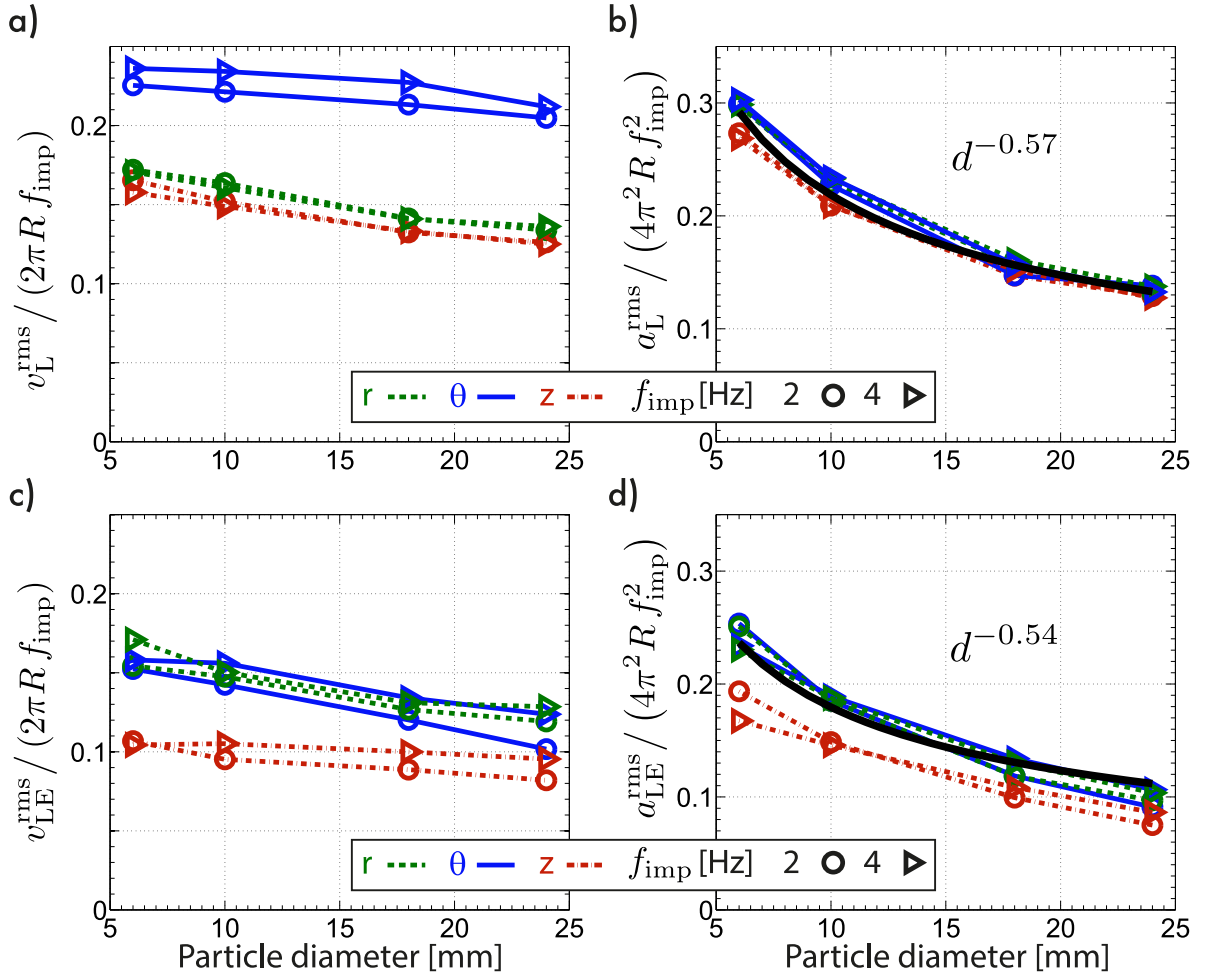
Figure 7. Standard deviation (root mean square values) of normalized quantities as a function of the particle diameter d for two impeller frequencies $f_{\text{imp}} = 2$ and $4\,\text{Hz}$. (a) Biased Lagrangian velocity components v_i^{rms}. (b) Biased Lagrangian acceleration components a_i^{rms}—the plain black line is a power-law fit in $d^{-0.56}$. (c) Unbiased Lagrangian velocity components v_i^{rms} using Eulerian conditioning and position PDFs weighting. (d) Unbiased Lagrangian acceleration components a_i^{rms} using Eulerian conditioning and position PDFs weighting—the plain black line is a power-law fit in $d^{-0.54}$.

Lagrangian tracer particles in the same flow [8]. It indicates that large particles no longer feel the dissipative scale η, and have an acceleration almost independent of the viscosity. As already observed in section 4.3, one can see in figures 7(b) and (d) that rms acceleration decreases more rapidly with increasing particle size than the rms velocity. When power laws are tested, one finds a behavior compatible with $a^{\text{rms}}(d)/f_{\text{imp}}^2 \propto d^\alpha$ and a scaling exponent close to $\alpha \simeq -0.5$. This is a larger variation than the $\alpha \simeq -1/3$ observed for smaller particles [7, 9]. Note that as the dissipation is nonhomogeneous in space, one may expect the exponent to depend on space so that the value $\alpha \simeq -0.65$ should be considered as a global estimate of the acceleration magnitude decrease. We also note that the measured exponent found in [9] was already larger than the one found in wind tunnel experiment [7], with a difference that can originate from the mean structure of the von Kármán flow.

6. Discussion and concluding remarks

The different maps, of position PDF, or those of velocity and acceleration fluctuations show the strong impact of the particle size on its dynamics. One can note an interesting correlation between position PDFs displayed in figure 3 and the maps of velocity fluctuations of figure 5(a). Particles with diameters 18 and 24 mm have position PDF maps qualitatively very similar to the color-inverted map of velocity fluctuations. This indicates that larger particles go preferentially in less active regions of the flow with smaller velocity and acceleration fluctuations. These results are in good agreement with turbophoresis, that is, the tendency of particles to migrate in the direction of decreasing turbulence level. However, particles are affected not only by velocity fluctuations, but also by the mean flow itself from which a trapping due to the mean pressure gradient may originate. An explanation for the preferential sampling of large particles could be that the decrease of acceleration fluctuations for large particles is not sufficient to overcome the trapping from the mean flow while smaller particles are less sensitive to the trapping as compared to turbulent fluctuations. Such an interpretation would lead to a trapping force per unit mass estimated as $F_{\text{trap}} \sim \partial_z \langle \overline{\mathbf{v}}_\theta \rangle^2 \sim 0.3 (4\pi^2 R f_{\text{imp}}^2)$ from mean flow profiles in figure 4(b). This trapping force could be compared to turbulent fluctuations of the mass force acting on neutrally buoyant particles estimated as $a_{\text{LE}}^{\text{rms}}(d)$ from figure 7(d). Comparing these two terms we find that $a_{\text{LE}}^{\text{rms}}(d)/F_{\text{trap}}$ decreases with d from 0.8 for 6 mm (nontrapped) particles to 0.3 for trapped particles of diameter 24 mm. This decrease of acceleration fluctuations may thus explain why large particles are more sensitive to the mean flow structure.

In order to investigate further the origin of this preferential sampling, we have varied many parameters concerning the flow (viscosity, amplitude of large-scale forcing) as well as the particles' characteristics (size, density and surface roughness). All these studies have confirmed the robustness of the preferential sampling effect with respect to parameter variations. No variation of the position PDFs has been observed, for a given size, when Reynolds number $Re = 2\pi R^2 f_{\text{imp}}/\nu$ has been varied by changing the discs velocity. This observation is consistent with the fact that, as reported in section 5, velocities and accelerations scale with the driving of the flow. Indeed, the relative intensity of trapping as compared to fluctuations is not modified in such a regime. This has been confirmed by recent experiments under not fully turbulent conditions with increased viscosity $\mu = 135\,\mu_{\text{water}}$ for which velocity fluctuations are decreased as compared to the mean flow [27]. In such a regime, trapping was found to increase on the sides of the measurement volume, near the flow poloidal neutral lines.

In order to investigate and possibly modify the rotation–translation coupling of the particle found in [10], the particle surface roughness was also varied and was shown to not modify the position PDFs.

Finally, several other experiments were done with similar particles (spheres of diameters $d = [6, 10, 18, 24]$ mm) while changing the density with respect to the fluid. Using water (unit density), experiments were performed using the same PolyAmid particles with density $\rho_{\text{PA}} = 1.14\,\text{g cm}^{-3}$ and lighter PolyPropylene particles with density $\rho_{\text{PP}} = 0.9\,\text{g cm}^{-3}$. These experiments also allowed us to investigate the influence of the viscosity of the fluid ($\mu = 7.5 \times 10^{-3}\,\text{Pa s}$ for the water–glycerol mixture versus $\mu = 1.0 \times 10^{-3}\,\text{Pa s}$ for distilled water). It was found that the relative density of the particle modified the position PDF maps, lighter particles being more efficiently trapped and heavier particles being slightly less trapped than neutrally buoyant ones of the same diameter. This can be understood in the framework of the beta-Stokes model of inertial particles dynamics [29], for which the influence of the mean pressure gradient is given by the reduced density ratio $\beta = 3\rho_f/(2\rho_p + \rho_f)$ through an

added mass force. This means that the average pressure gradient exerted on the solid particles together with velocity fluctuations felt by the particles are the key parameters to understand this preferential sampling effect. In the case of the turbulent von Kármán flow considered here, the preferential sampling occurs around the same axial positions as the flow poloidal neutral flow lines. These structures are stable attractors of the laminar von Kármán flow. It suggests that freely advected particles, when large enough compared to the dissipation scale, perform some average of the flow field and reveal its low-dimensional dynamics.

Acknowledgments

References

[1] Gatignol R 1983 *J. Méc. Théor. Appl.* **1** 143–60
[2] Maxey M R and Riley J J 1983 *Phys. Fluids* **26** 883–9
[3] Elghobashi S and Truesdell G C 1992 *J. Fluid Mech.* **242** 655–700
[4] Mordant N, Metz P, Michel O and Pinton J F 2001 *Phys. Rev. Lett.* **87** 214501
[5] Voth G A, Porta A L, Crawford A, Alexander J and Bodenschatz E 2002 *J. Fluid Mech.* **469** 121–60
[6] Toschi F and Bodenschatz E 2009 *Annu. Rev. Fluid Mech.* **41** 375–404
[7] Qureshi N M, Bourgoin M, Baudet C, Cartellier A and Gagne Y 2007 *Phys. Rev. Lett.* **99**
[8] Brown R D, Warhaft Z and Voth G A 2009 *Phys. Rev. Lett.* **103** 194501
[9] Volk R, Calzavarini E, Leveque E and Pinton J F 2011 *J. Fluid Mech.* **668** 223–35
[10] Zimmermann R, Gasteuil Y, Bourgoin M, Volk R, Pumir A and Pinton J F 2011 *Phys. Rev. Lett.* **106** 154501
[11] Klein S, Gibert M, Bérut A and Bodenschatz E 2013 *Meas. Sci. Technol.* **24** 024006
[12] Cisse M, Homann H and Bec J 2013 *J. Fluid Mech.* **735** R1
[13] Gasteuil Y, Shew W L, Gibert M, Chillà F, Castaing B and Pinton J F 2007 *Phys. Rev. Lett.* **99** 234302
[14] Zimmermann R, Fiabane L, Gasteuil Y, Volk R and Pinton J F 2013 *New J. Phys.* **15** 015018
[15] Zimmermann R, Gasteuil Y, Bourgoin M, Volk R, Pumir A and Pinton J F 2011 *Rev. Sci. Instrum.* **82** 033906
[16] Ouellette N T, Xu H, Bourgoin M and Bodenschatz E 2006 *New J. Phys.* **8** 102
[17] Marié L 2003 Transport de moment cinétique et de champ magnétique par un écoulement tourbillonnaire turbulent: influence de la rotation *PhD Thesis* Université Paris 7
[18] Monchaux R, Ravelet F, Dubrulle B, Chiffaudel A and Daviaud F 2006 *Phys. Rev. Lett.* **96** 124502
[19] Lopez-Caballero M 2013 Large scales in a von Karman swirling flow *PhD Thesis* University of Navarra
[20] de la Torre A and Burguete J 2007 *Phys. Rev. Lett.* **99** 054101
[21] Machicoane N, Bonaventure J and Volk R 2013 *Phys. Fluids* **25** 125101
[22] Zimmermann R 2013 How large spheres spin and move in turbulent flows *PhD Thesis* Université de Lyon
[23] Soille P 2003 *Morphological Image Analysis: Principles and Applications* (New York: Springer)
[24] Tsai R 1987 *IEEE J. Robot. Autom.* **3** 323–44
[25] Xu H 2008 *Meas. Sci. Technol.* **19** 075105
[26] Fiabane L, Zimmermann R, Volk R, Pinton J F and Bourgoin M 2012 *Phys. Rev.* E **86** 035301
[27] Ravelet F, Chiffaudel A and Daviaud F 2008 *J. Fluid Mech.* **601** 339–64
[28] Zocchi G, Tabeling P, Maurer J and Willaime H 1994 *Phys. Rev.* E **50** 3693–700
[29] Calzavarini E, Kerscher M, Lohse D and Toschi F 2008 *J. Fluid Mech.* **607** 13–24